Surface & Coatings Technology 424 (2021) 127638

Contents lists available at ScienceDirect

Surface & Coatings Technology

journal homepage: www.elsevier.com/locate/surfcoat

Time-averaged and time-resolved ion fluxes related to reactive HiPIMS deposition of Ti-Al-N films

L. Zauner [a,*], A. Bahr [a], T. Kozák [b], J. Čapek [b], T. Wojcik [a,c], O. Hunold [d], S. Kolozsvári [e], P. Zeman [b], P.H. Mayrhofer [c], H. Riedl [a,c]

[a] Christian Doppler Laboratory for Surface Engineering of high-performance Components, TU Wien, Austria
[b] Department of Physics and NTIS – European Center of Excellence, University of West Bohemia, Czech Republic
[c] Institute of Materials Science and Technology, TU Wien, Austria
[d] Oerlikon Balzers, Oerlikon Surface Solutions AG, Liechtenstein
[e] Plansee Composite Materials GmbH, Germany

ARTICLE INFO

Keywords:
Ti-Al-N
HiPIMS
Thin film
Mass spectroscopy
Time-resolved

ABSTRACT

Time-averaged and time-resolved ion fluxes during reactive HiPIMS deposition of $Ti_{1-x}Al_xN$ thin films are thoroughly investigated for the usage of $Ti_{1-x}Al_x$ composite targets – Al/(Ti + Al) ratio $x = 0.4$ and 0.6. Ion mass spectroscopy analysis revealed, that increasing x in the target material or reducing the N_2 flow-rate ratio leads to a proportional increase of the Al^+-ion count fraction, whereas that of Ti^{n+}-ions ($n = 1$, 2) remains unaffected despite of comparable primary ionisation energies between Al and Ti. In fact, energetic Ti^{2+}-ions account for the lowest flux fraction incident on the substrate surface, allowing for a high Al-solubility limit in cubic-structured $Ti_{1-x}Al_xN$ thin films ($x_{max} \sim 0.63$) at low residual stresses. In addition, time-resolved plasma analysis highlights the simultaneous arrival of metal- and process-gas-ions throughout the entire HiPIMS pulse duration. These ion-bombardment conditions, which were dominated by gas-ion irradiation with a significant contribution of Al^+-ions (up to ~20 %) and negligible energetic Ti^{2+}-ions, allowed for the growth of cubic $Ti_{0.37}Al_{0.63}N$ coatings exhibiting high indentation hardness of up to ~36 GPa at a low compressive stress level ($\sigma = -1.3$ GPa).

1. Introduction

The past decades in the development of plasma-based physical vapor deposition (PVD) techniques have meticulously focused on accessing innovative routes of controlled ion-bombardment during thin film growth [1–4]. Within this context, high-power impulse magnetron sputtering (HiPIMS) – a technological advancement to drastically enhance the flux of ionized target species involved in conventional DC magnetron sputtering (DCMS) – is rendered particularly attractive for introducing novel means of influencing working gas- and metal-ions incident on substrate and growing film [5–9]. HiPIMS utilises short (10–500 μs), yet highly energetic plasma discharges (up to several $kW{\cdot}cm^{-2}$) at relatively low repetition rates (tens of Hertz to kilo-Hertz) to generate significantly increased plasma densities on the target surface, thus leading to an enhanced fraction of ions present in the film-forming vapor [6,7]. The increased contribution of ions to thin film growth allows for an enhanced control over the energy delivered to the growing film, revealing new kinetic pathways of controlling the structure-property relationship [10–14]. Moreover, ion-driven phenomena such as process gas rarefaction, self-sputtering, or working gas recycling are characteristic for HiPIMS discharges, hence creating distinctly different process conditions when compared to DCMS, especially under reactive deposition environments [15–19]. Nevertheless, numerous studies already highlighted the beneficial impact of HiPIMS on thin film quality, producing densified microstructures, improved mechanical properties, reduced surface roughness, or enhanced film uniformity on complex shaped substrates [20–24].

Many of the advantageous aspects of HiPIMS are driven by or related to the dynamics of the ion distribution bombarding the growing film surface. Consequently, complementary detailed plasma analysis in the time- and energy-domain has evolved into a vital extension for such ion-based PVD techniques through unfolding the correlation between deposition parameters and ion distributions (*i.e.*, composition, energy, or temporal sequence) arriving on the substrate surface [11,25–33]. Utilising ion mass spectroscopy allows for methodically altering the incident ion composition – in conjunction with given deposition

* Corresponding author.
E-mail address: lukas.zauner@tuwien.ac.at (L. Zauner).

https://doi.org/10.1016/j.surfcoat.2021.127638
Received 2 August 2021; Received in revised form 17 August 2021; Accepted 18 August 2021
Available online 23 August 2021

parameters – and to identify the distinct influence of individual ionic species on the resulting thin film quality [34]. Moreover, combining a known temporal sequence of process gas- and metal-ions with a specially tailored substrate bias potential synchronised to a precise time-domain within the HiPIMS pulse, provides advanced pathways of controlling coating stoichiometry, film adhesion, and even phase formation during ion-assisted thin film growth [35–38].

Taking up the concept from Ref. [39], Nedfors *et al.* [40] have shown that using time- and energy-resolved ion mass spectroscopy in conjunction with a substrate bias synchronised to different time-frames of the HiPIMS discharge can be utilised to influence the average energy per deposited species $\langle E_D \rangle$ even when using a multi-element target. Moreover, specifically attracting film-forming constituents (there B^+-ions during the deposition of TiB_2) was demonstrated to mitigate Ar^+ incorporation, and thus also residual compressive stresses. A complementary work by Bakhit *et al.* [41] also highlighted an alternative approach of using time-dependent ion mass spectroscopy combined with decreasing HiPIMS pulse lengths to effectively control the B/Ti-ratio in a wide range for this thin films class.

Detailed *in-situ* plasma analysis during HiPIMS deposition of Al alloyed cubic TM-N-based coatings has further contributed to access additional pathways of maintaining, or even exceeding previously established solubility limits for these typically supersaturated cubic structures – *e.g.* the well-studied Ti-Al-N system [42,43]. This benchmark system exemplifies the capabilities of kinetically-limited film growth during PVD, providing excellent high hardness and wear protection when synthesised in the metastable face-centred cubic structure (*c*, B1, NaCl-prototype). Since the high-temperature oxidation resistance of *c*-$Ti_{1-x}Al_xN$ scales with the AlN mole fraction (x), a commonly adopted strategy is to maximise the Al/(Ti + Al)-ratio of the metal sublattice, while aiming to maintain the cubic structure type. Exceeding the solubility limit ($x_{max,} \sim 0.67$ for DCMS or arc evaporation), results in the precipitation of the thermodynamically stable hexagonal (*w*, B4, ZnS-wurtzite prototype) AlN phase, thus deteriorating both the thermal stability and mechanical properties [44–48]. In fact, most studies utilising reactive HiPIMS (R-HiPIMS) for the synthesis of $Ti_{1-x}Al_xN$ thin films reported on drastically reduced solubility limits compared to conventional plasma-based techniques [49–51].

Utilising a "hybrid" Al-DCMS/Ti-HiPIMS (and Al-HiPIMS/Ti-DCMS) approach, Greczynski *et al.* [34] identified the detrimental effect of energetic, doubly-charged Ti-ions on the structure of reactively deposited $Ti_{1-x}Al_xN$ thin films. It was demonstrated that lattice defects induced from intense Ti^{2+}-ion bombardment act as preferred nucleation sites for the wurtzite phase, causing a drastic reduction of x_{max}. Building on this concept, a novel synthesis route was developed where high temporal fluxes of Al^+-ions are specifically employed during a HiPIMS pulse to extend the metastable Al-solubility limit of *c*-TM-Al-N based coatings beyond values observed for conventional PVD techniques. By applying a high substrate bias synchronised to the Al-rich portion of the discharge, energetic Al^+-ions are incorporated into the *c*-TM-N host structure – referred to as "subplantation" – thereby effectively suppressing any diffusion driven precipitation of a second phase. This method was proofed successful especially for the V-Al-N system, where an increase of x_{max} from $x = 0.52$ to 0.75 could be achieved [36,52,53].

The common concept of these advances in the application of (*R*)-HiPIMS technology is built around a precise intersection between a detailed knowledge of the time- and energy-resolved ion distribution originating in the discharge and the structure-property relation of the deposited film. In this work, we present detailed results on the effect of altered deposition parameters on the ion flux distribution arriving at the substrate during R-HiPIMS deposition of $Ti_{1-x}Al_xN$ thin films by means of time- and energy-resolved ion mass spectroscopy. Different discharge conditions involving an increasing Al content in the powder-metallurgically prepared $Ti_{1-x}Al_x$ target ($x = 0.4$ and 0.6) as well as changing nitrogen flow rate ratios are employed. Variations observed in the average ion count fractions as well as the temporal sequence of the arriving ions are related to structural changes observed within the synthesised thin films. Furthermore, the thin films are analysed in more detail with respect to changes in morphology and local phase formation. Finally, the obtained results are discussed in relation to the mechanical properties of all $Ti_{1-x}Al_xN$ thin films investigated.

2. Experimental

Mass spectroscopy measurements were performed to investigate the composition, the energy, as well as the time-resolved sequence of ions incident on the substrate plane during HiPIMS sputtering of $Ti_{1-x}Al_x$ composite targets in various nitrogen containing atmospheres. Two different target compositions ($Ti_{0.6}Al_{0.4}$ and $Ti_{0.4}Al_{0.6}$; powder-metallurgically prepared, Plansee Composite Materials GmbH) were operated in varying N_2/Ar-mixtures, with the nitrogen flow-rate ratio $f^{norm}_{[N2]} = f_{[N2]}/(f_{[N2]} + f_{[Ar]})$ increased from 0, to 0.23, to 0.3, and 1. Prior to all measurements, the cylindrical vacuum system was pumped to a base pressure below $3{\cdot}10^{-4}$ Pa using a diffusion pump, while the total process gas pressure (p) was fixed to $p = 0.4$ Pa during magnetron operation. The system was equipped with a 4-in. cathode (Vtech, Gencoa Ltd), allowing for an *in-situ* control of the magnetic field configuration on the $Ti_{1-x}Al_x$ targets. Since the mass spectroscopy measurements could not be performed in the same chamber used for the subsequent deposition of $Ti_{1-x}Al_xN$ thin films, the magnetic field strength had to be adjusted to reproduce the waveforms of the target voltage $U_T(t)$ and the discharge current $I_D(t)$ observed during the deposition.

The magnetron was powered by a 5 kW plasma generator (ADL GmbH), with the HiPIMS signal modulated using a SIPP2000USB pulse power controller (Melec GmbH). For all measurements, the repetition frequency (f) and pulse duration (t_{on}) were maintained at 500 Hz and 75 μs, respectively, with the corresponding duty cycle $t_{on}/T = 3.75$ %, where the pulse period T equals $1/f$. The waveforms of the magnetron voltage and the discharge current were recorded on a digital oscilloscope (PicoScope 6403C, Pico Technology) utilising a voltage-(Testec TT-HV 150) and current-(Tektronix TCP303) probe. The average target power density in a pulse period was evaluated as

$$\overline{P} = \frac{1}{A_T \cdot T} \int_0^T U_T(t)\, I_D(t) dt$$

where A_T represents the total target area (~ 78.5 cm^2). The discharge peak power density within a period was calculated as

$$P_{pk} = max\left(\frac{U_T(t) \cdot I_D(t)}{A_T}\right)$$

with $U_{T,pk}$ and $I_{D,pk}$ denoting the target peak voltage and discharge peak current, respectively. In the presented experiments, the average power density was maintained constant at $\overline{P} \sim 10.25$ W/cm^2, resulting in peak power densities ranging from $P_{pk} \sim 0.5$ to 1 kW/cm^2, depending on $f_{[N2]}^{flow}$ used. Moreover, both the employed process gas as well as the HiPIMS discharge parameters were based on our recently published work [20].

Time-averaged ion energy distributions of positive ions in the discharge plasma were measured using an energy-resolved mass spectrometer (EQP 300, Hiden Analytical) with the sampling orifice placed parallel to the target surface at a fixed distance of $d = 110$ mm. A shutter construction was further placed in front of the mass spectrometer orifice, to allow for stable discharge conditions prior to all measurements performed. The mass spectrometer was tuned to $^{40}Ar^+$ ions and the obtained setting was kept fixed for all measurements. Standard time-averaged acquisitions of ion spectra were measured for $^{40}Ar^+$, $^{27}Al^+$, $^{27}Al^{2+}$, $^{14}N^+$, $^{28}N_2{}^+$, $^{48}Ti^+$ and $^{48}Ti^{2+}$ ions. The extractor voltage was set

to −10 V with respect to ground potential and the electrode controlling the ion energy was scanned from −5 to 80 V at a step size of 0.1 V ensuring that practically all ions (with different energies) were recorded during the measurement. The dwell time for ion detection at each point was 10 ms. The ion energy distribution for each species was recorded during five consecutive scans to increase the signal-to-noise ratio and to identify any potential long-term changes in the discharge conditions during data acquisition. Assuming consistent sensitivity of the instrument to ions at various energies, the total flux of all species was calculated by integrating the corresponding time-averaged energy distribution over the full energy range. The recorded counts for the $^{48}Ti^{n+}$ species were additionally corrected for natural isotope abundance ($^{48}Ti \sim 73.72$ % of all stable isotopes [54]). Moreover, $^{40}Ar^{+}$ and $^{48}Ti^{n+}$ species were corrected for system transmission using the manufacturers calibration data (transmittance of $^{40}Ar^{+} \sim 86.17$ % and $^{48}Ti^{+} \sim 76.02$ %, respectively [55]). Also, no indications for the molecular species $^{62}TiN^{+}$ and $^{41}AlN^{+}$ were found, hence their fluxes into the mass spectrometer are likely several orders of magnitude lower compared to the fluxes of metal ions. With the assumption of an identical transmission characteristic of the instrument for all species when implementing the corrections, the composition of the total flux of ions onto the substrate surface was calculated on the basis of these integral fluxes determined.

In addition, to obtain the temporal sequence of ions arriving at the substrate, time-resolved ion counts were recorded for specific HiPIMS discharge conditions. In that case, the mass spectrometer was set to continuously scan for one ion species in a narrow energy range (typically 20 eV) corresponding to the signal peak in the ion energy distribution function with a dwell time of 100 ms. The raw pulse-stream output of the ion detector was fed to a multichannel scaler (SR430, Stanford Research Systems). This device registered the incoming pulses and accumulated them successively in evenly spaced time intervals once a trigger signal for the negative voltage pulse of the HiPIMS power supply was registered. Thus, the time of ion arrival onto the detector with respect to the beginning of the negative pulse was discriminated with a time resolution of 1.28 µs (width of the accumulation time interval). A correction for the time-of-flight of ions in the mass spectrometer was applied during post-processing of the data [55,56]. Several tens of thousands of pulse periods were accumulated to increase the signal-to-noise ratio.

To analyse the influence of the recorded ion spectra on the thin film properties, $Ti_{1-x}Al_xN$ coatings were synthesised using a separate, in-house developed magnetron sputtering system holding two 6-in. cathodes equipped with identical $Ti_{1-x}Al_x$ composite targets as were used during the mass spectroscopy studies. The magnetrons (large circular, Gencoa Ltd.) were individually powered by a 5 kW HiPIMS plasma generator (HIP3, Solvix). The system uses a confocal, bottom-up configuration for the two cathodes resulting in an included angle of $\alpha = 20°$ between the target and substrate normal. All depositions were carried out with a fixed distance of $h = 110$ mm between the rotating substrate holder (0.25 Hz) and the target surface in alignment with the mass spectroscopy analysis. Further details on the deposition system can be extracted from [20].

Before each deposition, a base pressure below $3{\cdot}10^{-4}$ Pa was established. The $Ti_{1-x}Al_xN$ thin films were deposited on Si platelets ((100)-oriented, 20 × 7 × 0.38 mm^3), monocrystalline Al_2O_3 platelets ((1−102)-oriented, 10 × 10 × 0.53 mm^3), as well as polished austenite platelets (DIN EN 1.4571, 20 × 7 × 0.8 mm^3). Prior to all depositions, the substrate materials were pre-cleaned in an ultrasonic bath using acetone and isopropyl alcohol, consecutively. A 30 min heating sequence to a substrate temperature of $T_S = 300$ °C (measured directly on the substrate holder, corresponds to a heater temperature of $T_H = 500$ °C) was followed by a 10 min Ar-ion etching step conducted at a process pressure of $p_{etch} = 3$ Pa and a substrate potential of $U_S = -1000$ V. The discharge parameters and overall process conditions (*i.e.*, pulse frequency and duration, average power density, deposition pressure, nitrogen flow-rate ratios) for all $Ti_{1-x}Al_xN$ depositions were selected according to the settings used for the mass spectroscopy measurements. Details of the deposition conditions and coating properties are summarised in Table A1 of Appendix A.

Investigations on the coating structure were performed using X-ray diffraction (XRD) analysis on a PANalytical XPert Pro MPD system equipped with a Cu-Kα radiation source (wave length $\lambda = 1.54$ Å) in Bragg-Brentano geometry. The chemical composition of all $Ti_{1-x}Al_xN$ thin films was characterised utilising energy dispersive X-ray spectroscopy (EDS) in top-view configuration (EDAX EDS detector, 10 kV acceleration voltage). Furthermore, scanning electron microscopy (SEM, FEI Quanta 200, operated at 10 kV) was employed to investigate the coating morphology based on fracture cross-sections of single-side coated Si substrates. Additional analysis on local phase formation as well as growth characteristics of selected $Ti_{1-x}Al_xN$ thin films was obtained by transmission electron microscopy (TEM, FEI TECNAI F20) complemented by selected area electron diffraction (SAED). The evaluation of SAED diffractograms was conducted using the CrysTBox software package [57].

The mechanical properties including both the indentation hardness (H) and modulus (E) were characterised using an ultra-micro indentation system (UMIS) equipped with a Berkovich diamond indenter. For each coating, 30 load-displacement curves were recorded with the indentation load varied between 6 and 45 mN. The evaluation of the collected data was conducted according to the Oliver and Pharr method [58]. Residual macro-stresses within the $Ti_{1-x}Al_xN$ coatings were further calculated from the modified Stoney-equation combined with curvature measurements of single-side coated Si substrates obtained from optical profilometry (PS50, Nanovea) [59].

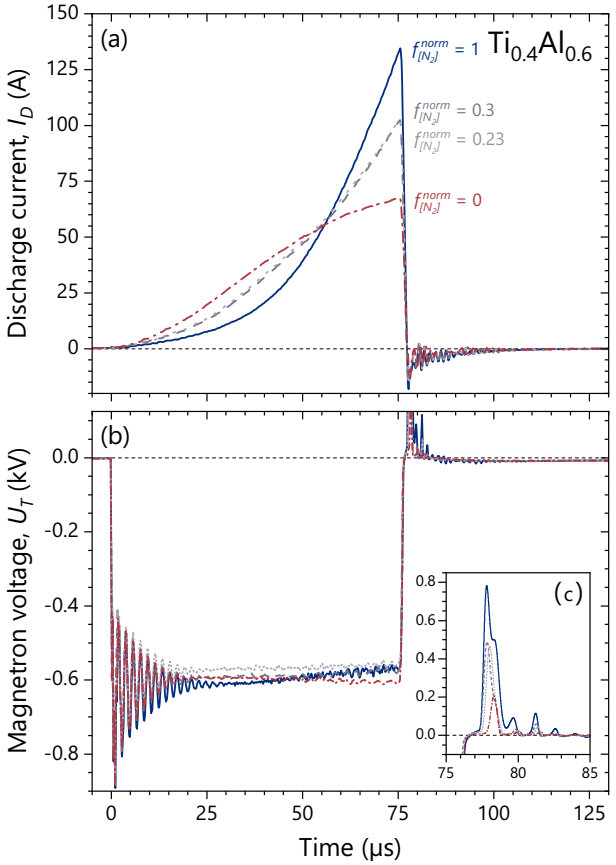

Fig. 1. Time-evolution of (a) the discharge current $I_D(t)$ and (b) the magnetron voltage on a $Ti_{0.4}Al_{0.6}$ target as functions of the applied nitrogen flow rate ratio $f^{norm}_{[N2]}$ for a pre-set pulse duration of 75 µs. Insert (c) shows details of the corresponding positive voltage overshoot recorded at the end of each pulse.

3. Results & discussion

3.1. Discharge characteristics

Fig. 1 shows the time-evolution of the discharge current $I_D(t)$ and the magnetron voltage $U_T(t)$ recorded during HiPIMS sputtering of a $Ti_{0.4}Al_{0.6}$ target in mixed N_2/Ar-atmospheres as functions of time. During all measurements, the discharge parameters were kept constant at $f = 500$ Hz, $t_{on} = 75$ µs, and $\overline{P} \sim 10.25$ W/cm^2, respectively, while $f^{norm}_{[N2]}$ was increased from 0 to 1. Irrespective of the nitrogen content in the atmosphere, the discharge current increases over time, reaching a respective maximum at the end of the pulse. When increasing the nitrogen flow-rate ratio from 0 to 0.23, the discharge current shifts from a logistic to an exponential growth until voltage shutdown at $t = 75$ µs, reaching values of $I_{D,pk} = 67$ and 103 A, respectively (see Fig. 1a). Upon further increasing $f^{norm}_{[N2]}$ to 0.3 and 1, the exponential characteristic is even more pronounced, with $I_{D,pk}$ increasing up to 135 A for the highest nitrogen content (corresponds to a peak current density of 1.72 A/cm^2). Concurrently, by increasing the nitrogen flow-rate ratio, the onset of the current rise becomes retarded and the initial slope of the waveforms is observed to be less steep. Moreover, the uniform evolution of the current waveforms suggests that no distinct contribution through working gas recycling and/or self-sputter recycling – indicated by a second maximum in $I_D(t)$ – occurs at higher peak current densities [7]. Since the average energy imparted into each pulse ($E_p = \overline{P}/f$) was constant for all experiments, the increasing peak current densities can be clearly attributed to the altered nitrogen flow-rate ratio, consequently shifting the $Ti_{1-x}Al_x$ composite target from a metallic to a more poisoned sputtering mode. Considering that the emission of secondary electrons is significantly amplified for AlN, and only marginally lowered for TiN, when compared to their pure metallic states, the increasing peak current densities can be explained by the progressive formation of surface nitrides upon increasing $f^{norm}_{[N2]}$ [60]. Moreover, self-sputtering of the nitrided target surface by energetic N^+-ions at high values of $f^{norm}_{[N2]}$ additionally supports the emission of secondary electrons [61].

Following typical oscillations after the discharge ignition, the magnetron voltage is almost constant throughout the pulse for all nitrogen variations conducted, resembling an almost ideal rectangular signal with $U_T \sim -600$ V (see Fig. 1b). The magnetron shutdown at $t = 75$ µs is accompanied by a steep decrease in the applied potential, followed by a 3–5 µs long positive "overshoot" of the magnetron voltage of up to +800 V for $f^{norm}_{[N2]} = 1$ (see insert c). This application of a positive voltage after the HiPIMS pulse derives from the inherent inductance of the power supply used, where the voltage amplitude can be estimated by the following expression:

$$V^+ \propto L \cdot \frac{dI_{D,pk}}{dt}$$

Through this almost instantaneous inversion in magnetron polarity and the resulting difference in plasma and substrate potential, ions located in the vicinity of the target get accelerated towards the substrate plane at energies corresponding to the positive pulse voltage [12].

The measurements were repeated for a $Ti_{0.6}Al_{0.4}$ target (see Fig. A1 in Appendix A) with an identical stepwise increase of the nitrogen flow-rate ratio from 0 to 1, revealing analogous results for both the evolution of the discharge current and magnetron voltage. For a pure Ar-atmosphere, a similar peak current of ~70 A is recorded at the end of the pulse. However, upon increasing $f^{norm}_{[N2]}$ to 0.23 and further, no intermediate target poisoning state can be observed, instead the discharge current immediately saturates at peak values around 135 A. Hence, it can be concluded that upon increasing the Ti/Al-ratio within the target material, less nitrogen will be required to transfer the target to a fully poisoned state under the same HiPIMS conditions, being in perfect agreement with previous observations for DCMS. Moreover, both the magnetron voltage as well as the positive "overshoot" after the pulse were recorded at similar values with $U_T \sim -600$ V and $V^+_{max} \sim 800$ V, when compared to the $Ti_{0.4}Al_{0.6}$ target and the corresponding nitrogen flow-rate ratios.

3.2. Time-averaged composition of the total ion flux

In Fig. 2, the individual fractions of the ionic species as well as the overall composition of the total ion flux measured at a distance of $d = 110$ mm from the magnetron source is presented for all nitrogen flow-rate ratios applied for both $Ti_{1-x}Al_x$ target compositions. The obtained results provide qualitative information on the fractional changes in the total ion flux arriving at the substrate surface with respect to the nitrogen flow-rate variations. Here it should be noted, that the contributions from Al^{2+}- and N^+-ions cannot be separated due to an intensity overlap in the recorded spectra ($m/e = 13.5$ and 14, respectively). However, experiments in pure Ar atmosphere showed that Al^{2+}-signals are insignificant compared to those from Al^+-ions, hence they were not considered in the evaluation even at higher peak current densities with increasing $f^{norm}_{[N2]}$. This is in agreement with previous observations for HiPIMS powered Al targets and mainly related to the considerably

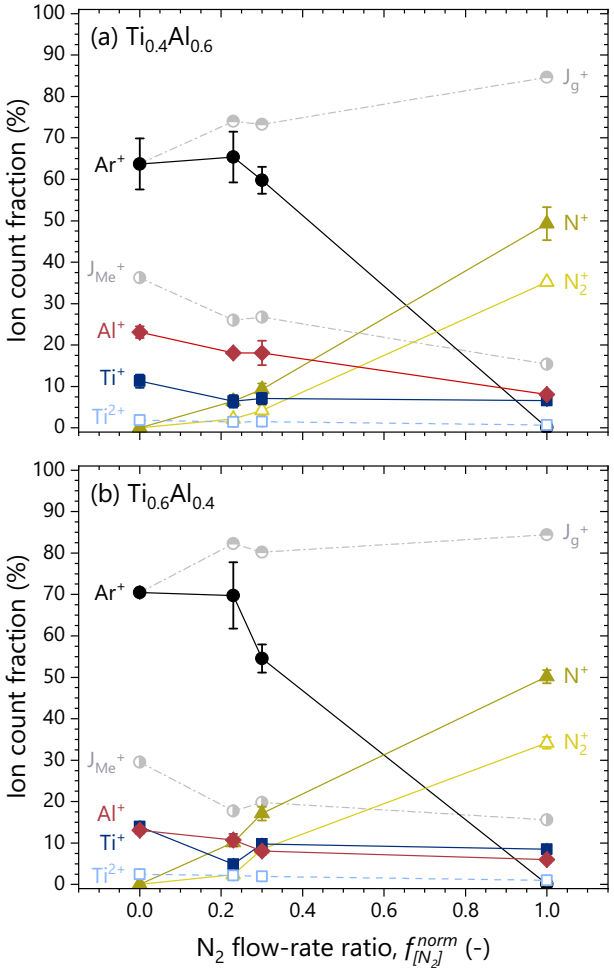

Fig. 2. Integral ion count fractions of the ionic species arriving at the substrate plane as function of the nitrogen flow rate ratio $f^{norm}_{[N2]}$, presented for (a) a $Ti_{0.4}Al_{0.6}$ and (b) a $Ti_{0.6}Al_{0.4}$ target, respectively. The data was acquired at a distance of $d = 110$ mm from the target surface. Singly charged species are presented by filled symbols and solid lines, whereas doubly charged ions are presented by open symbols and dashed lines. In addition, (a) and (b) contain the total flux of process gas ions J_{g^+} and metal ions J_{Me^+}, indicated by half-filled circles and dot dashed lines.

higher secondary ionisation energy of aluminium (IP_2^{Al} = 18.83 eV) compared to the primary ionisation energy of argon (IP_1^{Ar} = 15.76 eV) [34,54]. In addition, Fig. 3 presents a direct comparison of the flux compositions recorded at $f_{[N2]}^{norm} = 0.3$, for both the $Ti_{0.4}Al_{0.6}$ (blue, filled bars) and $Ti_{0.6}Al_{0.4}$ (red, dashed bars) target.

Over the entire range of $f_{[N2]}^{norm}$ considered, the flux of process gas ions J_{g^+} (*i.e.*, the combined flux of Ar^+, N_2^+, and N^+ ions) dominates the composition of the total ion flux emitted from the plasma discharge. In pure argon-atmosphere, the integral flux of metal ions J_{Me^+} (*i.e.*, the combined flux of Al^+, Ti^+, and Ti^{2+} ions) constitutes 36.3 and 29.6 % within the total ionic species ejected from the $Ti_{0.4}Al_{0.6}$ and $Ti_{0.6}Al_{0.4}$ target, respectively. Upon stepwise increase to pure nitrogen-atmosphere at $f_{[N2]}^{norm} = 1$, the corresponding values for J_{Me^+} decrease almost linearly to 15.4 and 15.6 %, respectively. This reduction in the metal-to-gas ion flux ratio J_{Me^+}/J_{g^+} – from 0.57 to 0.18 for the $Ti_{0.4}Al_{0.6}$ target and from 0.42 to 0.18 for the $Ti_{0.6}Al_{0.4}$ target – with increasing nitrogen flow results from a progressive nitride formation on the target surface, and hence a decreasing sputter yield of the metal constituents. In addition, the higher overall sputter yield of the $Ti_{0.4}Al_{0.6}$ target compared to the $Ti_{0.6}Al_{0.4}$ target – the sputter yield of Al is nearly twice that of Ti [62] – results in higher values of J_{Me^+} throughout all nitrogen flow rates.

The poisoning behaviour of the target material is of course strongly related to the Ti/Al-ratio and driven by the difference in the formation energy of the respective nitrides (−305.6 kJ/mol for TiN *vs.* -241.6 kJ/mol for AlN) [46,63]. This implies that the higher Al-containing $Ti_{0.4}Al_{0.6}$ target can sustain the metallic sputtering behaviour up to higher values of $f_{[N2]}^{norm}$ than the $Ti_{0.6}Al_{0.4}$ target, as seen in the current waveforms presented in Figs. 1 and A1. Accordingly, for $f_{[N2]}^{norm} = 0.23$ and 0.3 the data also show an increased population of N_2^+ and N^+ ions for the $Ti_{0.6}Al_{0.4}$ target due to less absorption of reactive gas (*i.e.,* a more poisoned target for the same N_2 flow rate), leading to a higher partial pressure and thus ionisation probability for the nitrogen species (see Figs. 2 and 3). In addition, for both target-types a predominance of N^+-ions (dark-yellow, filled triangles) over N_2^+-ions (light-yellow, open triangles) is observed in all flux compositions. This highlights the preferred ionisation of atomic N sputtered from the nitrided target surface as well as the promoted dissociation of N_2-molecules within the dense plasma created for high values of P_{pk} close to 1 kW/cm^2 (see Fig. 2).

Regarding the individual contribution of metal ions generated in the discharge, the data presented in Fig. 2a and b shows that Al^+-ions (red diamonds) account for a major fraction within J_{Me^+}, irrespective of the Al/Ti-ratio in the target material or $f_{[N2]}^{norm}$. Especially for the $Ti_{0.4}Al_{0.6}$ target, high values of J_{Al^+} up to 23 % of the total ion flux are observed in pure Ar-atmosphere (see Fig. 2a). Increasing the nitrogen flow to $f_{[N2]}^{norm}$ = 0.23 and 0.3 – being typical values for the deposition of Ti-Al-N thin films – the fraction of Al^+-ions in the sputtered flux decreases slightly to $J_{Al^+} \sim 18$ %. Following a near linear trend, this value further decreases down to $J_{Al^+} \sim 8.1$ % for $f_{[N2]}^{norm} = 1$. Contrary, fluxes for singly (dark-blue squares) as well as doubly (light-blue open squares) charged titanium ions remain almost unaffected by the N_2 flow-rate ratio, with J_{Ti^+} and $J_{Ti^{2+}}$ accounting for values below 14 % and 3 % within the total ionic flux from both targets, respectively.

Upon further comparison of J_{Al^+} to the combined flux of process gas ions J_{g^+} for both target chemistries, the increased ionisation of Al-atoms within the $Ti_{0.4}Al_{0.6}$ discharge is predominantly realised at the expense of a less efficient ionisation of the process gas species (see Figs. 2 and 3). This effect could be explained by an enhanced gas rarefaction occurring in front of the higher Al-containing target due to an increased density of metal species entering the plasma – mind the difference in sputter yield Al *vs.* Ti – thus resulting in a higher probability for atomic collisions and gas heating [16]. In addition, the significantly lower ionisation energy of aluminium atoms (IP_1^{Al} = 5.99 eV [54]) over the gaseous species (IP_1^{Ar} = 15.76 eV, IP_1^{N} = 14.53 eV, and IP_1^{N2} = 15.58 eV [54]) results in quenching of the electron energy distribution, thereby further contributing to a less efficient ionisation of process gas atoms [29,35]. This explanation is further underlined when reconsidering the evolution of both J_{Ti^+} and $J_{Ti^{2+}}$ between the two target compositions, revealing negligible differences despite the significant changes in J_{Me^+}/J_{g^+} over the entire N_2 flow range considered.

Consequently, it can be concluded that increasing the Al content in a $Ti_{1-x}Al_x$ composite target can be utilised for amplifying the fraction of Al^+ ions present in the sputtered flux, while reducing the overall fraction of process gas ions. Although a high Al/Ti ratio in a composite target also has to be considered with respect to phase formation and general solubility limits for the deposition of cubic structured $Ti_{1-x}Al_xN$ thin films, this provides a means of tuning J_{Al^+} while maintaining J_{Ti^+}, and especially the detrimental $J_{Ti^{2+}}$, low.

3.3. Time-resolved composition of the total ion flux

In order to study the temporal sequence of ions impinging on the substrate plane – especially from the aspect of time domains with high values of J_{Me^+}/J_{g^+} – time-resolved ion mass spectroscopy was performed

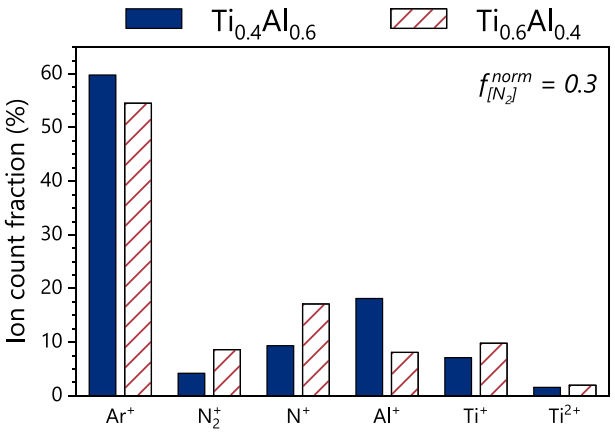

Fig. 3. Integral ion count fractions of the total ionic flux emitted from a HiPIMS discharge for a nitrogen flow rate ratio of $f_{[N2]}^{norm} = 0.3$, presented for both a $Ti_{0.4}Al_{0.6}$ (blue, filled bars), as well as a $Ti_{0.6}Al_{0.4}$ (red, dashed bars) target.

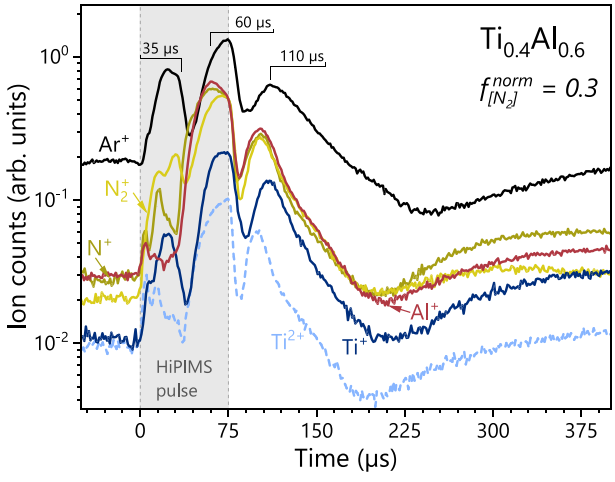

Fig. 4. Normalised time-evolution of the energy-integrated total ionic flux emitted during HiPIMS sputtering of a $Ti_{0.4}Al_{0.6}$ target, measured at $f_{[N2]}^{norm} = 0.3$ and a distance of d = 110 mm from the target. Singly charged species are presented by solid lines, whereas doubly charged ions are presented by dashed lines.

for a specific discharge condition. In Fig. 4, all major ion fluxes (Ar^+, Al^+, N^+, N_2^+, Ti^+ and Ti^{2+}) emitted from the $Ti_{0.4}Al_{0.6}$ target were recorded at the substrate position ($d = 110$ mm) for a nitrogen flow-rate ratio of $f^{norm}_{[N2]} = 0.3$. The total number of ion-counts normalised to the number of recorded pulse cycles is shown as a function of the time delay with respect to the voltage application to the magnetron.

Regarding the flux chemistry prior to the pulse ignition ($t < 0$ μs) – comprised of the residual ionized species from the previous pulse – a predominance of Ar^+ ions over the flux of N_2^+, N^+, Al^+, Ti^+ and Ti^{2+} ions is observed, with the latter two species accounting for the lowest fractions. Upon pulse ignition ($t = 0$ μs), and thus a rapid increase in the electron temperature T_e, all flux signals – especially the process gas ions – immediately gain intensity until reaching a first maximum at $t \sim 25$ μs. Since the ionic species generated in the target vicinity will require at least several tens of μs before arriving at the analyser, this initial influx of ions corresponds to ions created close to the mass spectrometer orifice by the first wave of energetic electrons [64]. In the following time interval until the cathode shutdown at $t = 75$ μs, the ion intensities increase to their respective maximum due to the arrival of ions generated within the main magnetron discharge – to approximately one order of magnitude higher than the corresponding initial values at $t = 0$ μs – coinciding well with $I_{D,pk}$ (see Fig. 1). Interestingly, the fluxes of metal ions J_{Me^+} and N^+-ions show a concomitant increase to their respective maximum at $t \sim 60$ μs, indicating that the latter species originates strongly from sputtering of target surface nitrides. Still, it should be noted that the highly dense plasma additionally contributes to the dissociation of N_2-molecules, thus explaining the extended N^+ peak. Contrary, fluxes for Ar^+- and N_2^+-ions show a slightly delayed arrival with an intensity maximum at $t = 75$ μs, suggesting for the ionisation to occur preferably in the bulk plasma.

After reaching the peak ion flux at the end of the 75 μs pulse, an abrupt decay of all ion signals can be observed, suggesting for a decrease in the number of arriving ions. However, this loss of ion intensity is due to a temporal broadening of the ion energy distribution function (IEDF) due to the positive voltage overshoot occurring on the magnetron at $t \sim 78$ μs (see insert c in Fig. 1, $U_T \sim 500$ V). The application of this positive pulse accelerates ions in the target proximity towards the analyser and the bulk plasma potential increases significantly, as it is always more positively charged than the most positive electrode within the plasma – represented by the magnetron during this time frame. Consequently, all ions obtain kinetic energies beyond the respective scanning range by this instantaneous difference between plasma and mass spectrometer potential, causing the apparent dip in the ion count evolution. This effect of a positive pulse on the IEDF is also described in more detail in recent studies by Kozak *et al.* [11] and Santiago *et al.* [12]. So in fact, the presented ion counts can be rather understood as obtaining a smooth decay between the shown maxima at $t = 75$ and 110 μs for all species. Finally, in the time domain of $t > 80$ μs ($U_T \sim 0$ V), the IEDFs gradually collapse, resulting in the recorded ion counts to slightly regain intensity up to $t \sim 110$ μs, to then decay at an equal rate in the following 150 μs until the initial state between the HiPIMS pulses is attained.

A further interesting observation when considering the collective evolution of all ion signals is that the relative flux composition is preserved throughout the entire pulse duration, with J_{Me^+}/J_{g^+} remaining fairly unchanged except for a slight dip at $t \sim 35$ μs due to the large influx of initial Ar^+ ions. Hence, no time domain obtaining a preferred arrival of either metal or process gas ions can be identified – resulting from well-known effects such as process gas rarefaction or quenching of T_e [16,28,35]. This continuous arrival of J_{Me^+} and J_{g^+} has direct implications on the deposition process, thereby minimising the controllability of film growth kinetics through synchronised metal-ion irradiation when using a $Ti_{1-x}Al_x$ composite target in a reactive HiPIMS process. Moreover, analogous to the results obtained for the integral ion flux (see Figs. 2 and 3), both J_{Ti^+} and $J_{Ti^{2+}}$ constitute the lowest fractions during the entire pulse period with respect to the total ionic flux, and in particular J_{Al^+}. This is especially interesting, when taking the moderate first ionisation energy of titanium ($IP_{Ti} = 6.83$ eV) – which is close to that of Al, yet significantly lower when compared to the present process gas species – as well as the almost equiatomic target composition into account [54]. Nevertheless, the presented results clearly underline our previous observations outlined in Ref. [20], where synchronising the bias potential to the HiPIMS pulse showed only minor effects on the phase formation of cubic structured Ti-Al-N.

3.4. Phase formation and chemical composition

Fig. 5a and b – containing the XRD diffractograms of films deposited from $Ti_{0.6}Al_{0.4}$ or $Ti_{0.4}Al_{0.6}$ targets, respectively – show the influence of different target chemistries and the nitrogen flow-rate ratio $f^{norm}_{[N2]}$ on the cubic phase stability of $Ti_{1-x}Al_xN$. In addition, Fig. 5c and d contain the corresponding chemical composition to the coatings presented in Fig. 5a and b, with square data points indicating the Al/(Ti + Al) ratio on the metal sublattice (lower axis) and circular data points denoting the nitrogen content (upper axis).

For a $Ti_{0.6}Al_{0.4}$ target chemistry (Fig. 5a and c), altering $f^{norm}_{[N2]}$ from 0.23 to 1.0 results in a slight decrease in the Al-content from $x = 0.46$ to 0.42 of the purely *fcc*-structured $Ti_{1-x}Al_xN$ thin films. This decrease can be understood based on the previously discussed difference in the heat of

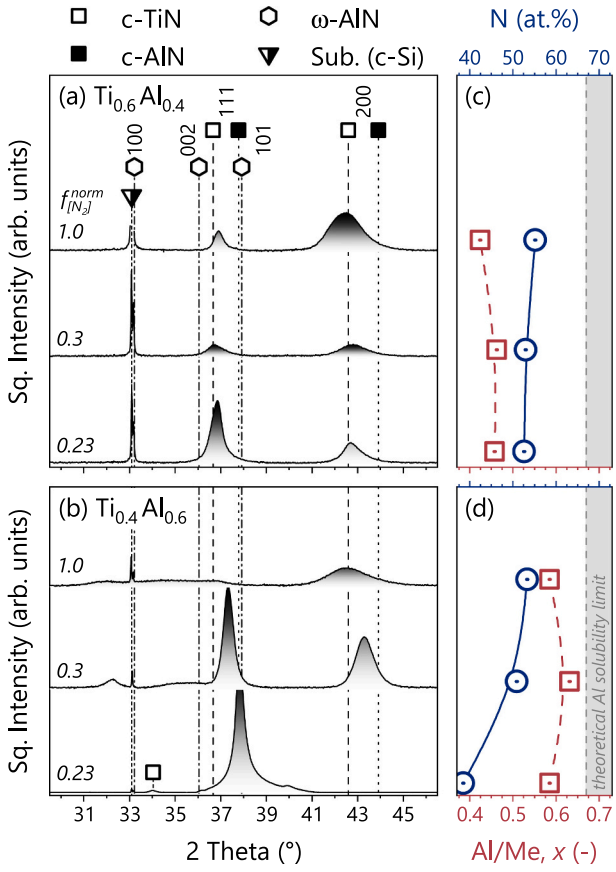

Fig. 5. (a) and (c) show XRD diffractograms of $Ti_{1-x}Al_xN$ thin films deposited from two 6-in. $Ti_{0.6}Al_{0.4}$ and $Ti_{0.4}Al_{0.6}$ cathodes, respectively, arranged with increasing $f^{norm}_{[N2]}$ from bottom (0.23) to top (1.0). The 2θ peak positions for cubic structured TiN (open square, [69]) and AlN (filled square, [70]), wurtzite AlN (open hexagon, [65]) and the substrate material (cubic Si, half-filled triangle, [71]) are indicated in (a) and (c). Furthermore, (b) and (d) show the chemical composition of all $Ti_{1-x}Al_xN$ thin films presented in (a) and (c), respectively – bottom axis Al/Me-ratio (red squares) and top axis N-content (blue circles) – with the data points aligned horizontally with the corresponding XRD diffractogram.

formation for TiN and AlN (see Section 2), the Al target particles commonly show a retarded poisoning state over the Ti particles, thus leading to a preferential Al sputter erosion at lower nitrogen flow rates [46,63]. Also, the N-content on the non-metal sublattice increases accordingly from 52 to 55 at.%, due to the higher availability of N^+- and N_2^+-ions in the plasma (see Fig. 2b) as well as the concomitant decrease in deposition rate at higher values of $f_{[N2]}^{norm}$ – the latter decreasing from 22.1 to 17.4 to 10.8 nm/min. Moreover, with increasing reactive gas flow $f_{[N2]}^{norm}$ from 0.23 to 1, the XRD diffractograms present a transition from a preferred (111)-oriented growth, to a randomly oriented growth with diminishing peak intensities (*i.e.*, smaller coherently diffracting domain sizes), towards a slightly preferred (200)-oriented growth.

In the case of the higher Al containing target $Ti_{0.4}Al_{0.6}$ (see Fig. 5b), the Al metal-fraction of the $Ti_{1-x}Al_xN$ thin films is $x = 0.59$ for a low and high $f_{[N2]}^{norm}$ of 0.23 and 1, while it increases to $x = 0.63$ at $f_{[N2]}^{norm} = 0.3$ (see Fig. 5d). Also, this behaviour is the result of selective poisoning processes of the Ti-Al target. With increasing $f_{[N2]}^{norm}$ from 0.23 to 0.30, the sputter yield of Ti decreases faster than that of Al (as Ti is more affine to N than Al and thus poisons earlier). However, if $f_{[N2]}^{norm}$ is sufficiently high to also poison Al, the reduction in sputter yield is more severe for Al due to the electrically isolating nature of AlN. The XRD diffractogram of the highest Al-containing coating ($x = 0.63$), prepared at $f_{[N2]}^{norm} = 0.3$, depicts a predominantly face-centered cubic structure having a preferred (111)-oriented growth, with slight indications for an additional wurtzite AlN-based phase (see the XRD peaks at $2\theta \sim 32.2°$ and 35°). The offset of these peaks from the ideal *w*-AlN reference pattern [65] hints towards the formation of a *w*-$Al_xTi_{1-x}N$ solid solution [44,47]. Reducing $f_{[N2]}^{norm}$ from 0.3 to 0.23 promotes the growth of a highly (111)-oriented cubic phase (even leading to the formation of the $K_{\beta 1}$ diffraction spot at $2\theta \sim 34°$). This *c*-$Ti_{0.41}Al_{0.59}N$ thin film is understoichiometric with a nitrogen content close to 40 at.%. The diffractogram further shows a clear shift towards the *c*-AlN reference line – despite an actual reduction in the aluminium content – indicative of a reduced compressive stress state and nitrogen deficiency. This drastic transition in film growth characteristics is in excellent agreement with previous studies [20,46] and follows the suggestions by Gall *et al.* [66], that a reduced availability of excess nitrogen (see Fig. 2a) yields a preferred growth in the (111)-direction. An increase of $f_{[N2]}^{norm}$ to 1 results in a multi-phased coating of (200)-oriented *c*-$Ti_{1-x}Al_xN$ and an almost X-ray amorphous *w*-$Al_xTi_{1-x}N$. Analogous to the coatings prepared from the lower Al containing target, increasing $f_{[N2]}^{norm}$ drastically reduces the deposition rate – from 66.2 to 50.6 to 10.9 nm/min. This allows for a less disturbed surface diffusion and provides more time for the growing film to approach the thermodynamically favoured crystal structures (cubic for Ti-rich and wurtzite for Al-rich). Moreover, the increased bombardment with N^+/N_2^+-ions (see Fig. 2a) additionally contributes to the wurtzite phase growth, hence the reduction in cubic phase fraction when increasing $f_{[N2]}^{norm}$ from 0.3 to 1.0 despite the concomitant reduction of the Al/(Ti + Al) ratio [46]. The competitive growth between *c*-TiN and the preferred *w*-AlN phase then results in a nano-composite structure [20]. Overall, the coatings prepared with $f_{[N2]}^{norm} = 0.23$ and 0.3 (Fig. 5b) provide significantly higher diffracted peak intensities when compared with the corresponding films prepared from the Ti-richer $Ti_{0.6}Al_{0.4}$ target (Fig. 5a), indicating altered film growth pathways when increasing the Al content in the target. Taking the ion count fractions presented in Fig. 3 into account, the increased bombardment with medium energetic Al^+-ions in favour of less Ti^{n+}- and N^+/N_2^+- species in the film forming flux contributes to enhanced surface diffusion and thus larger coherently diffracting domain sizes, which is also in good agreement with previous observations [20,49].

3.5. Growth morphology and phase formation

The $Ti_{1-x}Al_xN$ thin films were investigated in more detail with respect to growth morphology and phase formation by means of cross-sectional SEM and TEM, see Fig. 6. The fracture cross-sectional SEM image of $Ti_{0.54}Al_{0.46}N$ (Fig. 6a) shows a dense and highly columnar growth morphology, which is also underlined by the bright- (BF) and dark-field (DF) TEM investigations (Fig. 6b). Furthermore, the corresponding SAED studies taken in the interface near region (Fig. 6c1) as well as close to the film surface (Fig. 6c2) confirm the polycrystalline face-centred cubic crystal structure observed by XRD (Fig. 5a, pattern in the middle) – *i.e.,* with no preferred orientation – by ring-type diffraction patterns throughout the coating thickness. Investigations of the $Ti_{1-x}Al_xN$ coatings synthesised from the Al-richer $Ti_{0.4}Al_{0.6}$ target (Fig. 6d till l) nicely depict the influence of the increasing $f_{[N2]}^{norm}$ on the growth characteristics of these higher Al containing thin films. Both, the SEM fracture cross-sections as well as the corresponding BF- and DF-TEM images indicate the transition from a highly oriented $Ti_{0.41}Al_{0.59}N$ coating (N content of ~40 at.%) with large columnar crystals at $f_{[N2]}^{norm} = 0.23$ (see Fig. 6d, e, and f), to a slightly less preferred-oriented $Ti_{0.37}Al_{0.63}N$ coating at $f_{[N2]}^{norm} = 0.3$ with shorter columnar crystals (see Fig. 6g, h and i). A further increase in $f_{[N2]}^{norm}$ to 1.0 leads to the formation of an even finer microstructure, exhibiting a featureless morphology during SEM (Fig. 6j) with small-sized slightly elongated grains (Fig. 6k). The selected area electron diffraction patterns in Fig. 6f1 and f2 recorded for the $Ti_{0.41}Al_{0.59}N$ coating at $f_{[N2]}^{norm} = 0.23$ confirm the cubic crystal structure suggested by XRD (despite the N sub-stoichiometry) and show the highly crystalline nature of this coating through distinct point type diffractions, especially during later growth stages (see inset f2). Interestingly, the SAED investigations of the $Ti_{0.37}Al_{0.63}N$ coating prepared with $f_{[N2]}^{norm} = 0.3$ show that the wurtzite $Al_xTi_{1-x}N$ phase – as also observed during XRD, Fig. 5c – merely prevails in the interface near region (Fig. 6i1), whereas the main part of the coating is essentially cubic structured (Fig. 6i2). Since the deposition temperature was chosen rather low at $T_S \sim 300$ °C, this effect could be seen in progressive substrate heating due to the interaction with the dense HiPIMS plasma combined with enhanced ion bombardment. Certainly, these results show that the cubic $Ti_{1-x}Al_xN$ structure is accessible from $Ti_{1-x}Al_x$ compound targets even up to $x \sim 0.63$ (*i.e.*, close to the theoretical solubility limit) and despite the presence of doubly charged Ti-ions in the film forming flux. Again, in accordance with the XRD investigations (Fig. 5c), detailed SAED analyses of the coating synthesised with $f_{[N2]}^{norm} = 1.0$ underline the formation of cubic and wurtzite phases (see Fig. 6 l1-l2).

3.6. Mechanical properties

Finally, in addition to the structural and morphological changes discussed from the aspect of changing deposition and HiPIMS discharge conditions, the consequential influence on the mechanical properties of all $Ti_{1-x}Al_xN$ thin films was studied. Fig. 7a-c summarize the biaxial residual stresses, hardness, and indentation modulus for the coatings prepared from the two different targets as function of $f_{[N2]}^{norm}$, respectively. Single-phase cubic $Ti_{1-x}Al_xN$ coatings on Si substrates – sputtered using $Ti_{0.6}Al_{0.4}$ targets (red, filled squares) – exhibit compressive stresses between −1.2 and −2.5 GPa, with the lowest value observed for the fully polycrystalline $Ti_{0.53}Al_{0.46}N$ when using $f_{[N2]}^{norm} = 0.3$ (see Figs. 6a–c and 7a). The corresponding nanoindentation measurements give high hardness values, decreasing from $H = 36.4 \pm 1.5$ to 32.6 ± 2.5 GPa with increasing $f_{[N2]}^{norm}$, whereas the indentation modulus remains at $E \sim 420$ GPa almost unaffected by the nitrogen flow rate ratio variation, Fig. 7b

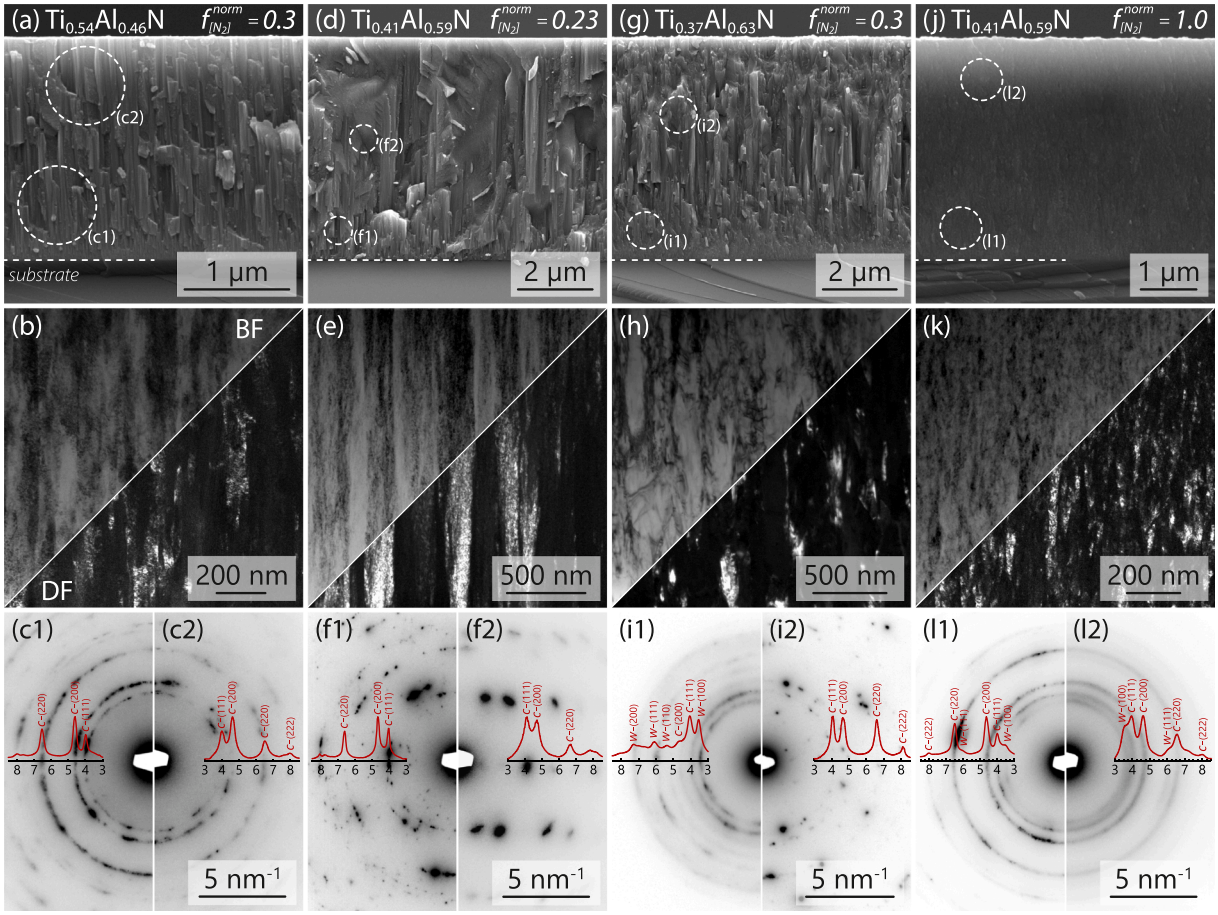

Fig. 6. (a), (d), (g), and (j) show SEM fracture cross-sections including the film chemistry and $f_{[N2]}^{norm}$ of selected $Ti_{1-x}Al_xN$ thin films from Fig. 5. (b), (e), (h), and (k) present bright- and dark-field TEM micrographs of the corresponding film cross-sections depicted in (a), (d), (g), and (j). The respective SAED diffractograms taken in the interface near region are shown in (c1), (f1), (i1), and (l1), whereas (c2), (f2), (i2), and (l2) contain SAED diffractograms recorded closer to the film surface, as indicated by the circles in (a), (d), (g), and (j). In addition, all SAED diffractograms contain an azimuthal integration of the pattern.

and c, respectively. Analogous to the findings in our previous work, the continuous reduction in hardness with increasing $f_{[N2]}^{norm}$ can be attributed to the increased fraction of nitrogen ions bombarding the film surface (see Fig. 2b) – thus leading to a weaker grain boundary structure [20,67]. Upon increasing the Al content in the target material to $Ti_{0.4}Al_{0.6}$ (see Fig. 7, blue, open squares) the obtained coatings exhibit biaxial compressive stresses which increase from −0.4 to −2.5 GPa with increasing $f_{[N2]}^{norm}$ from 0.23 to 1.0, respectively. A maximum hardness of 36.1 ± 3.5 GPa is obtained for the predominantly cubic structured $Ti_{0.37}Al_{0.63}N$ thin film prepared at $f_{[N2]}^{norm} = 0.3$. The minor wurtzite phase content of this coating is essentially present only at the near substrate region (Fig. 7i), thus its contribution to the hardness measurement can be neglected. Whereas preparing the film with $f_{[N2]}^{norm} = 0.23$ results in an understoichiometric phase, too much N_2 ($f_{[N2]}^{norm} = 1.0$) favours the formation of a significant amount of the wurtzite phase. Both scenarios lead to lower hardness (~ 29.5 GPa) and indentation modulus (380 ± 10 and 300 ± 9 GPa), Fig. 7b and c, respectively. Interestingly, when compared with conventional DCMS or cathodic arc evaporation (CAE) techniques, all $Ti_{1-x}Al_xN$ coatings obtained here have relatively low compressive stresses – especially at $f_{[N2]}^{norm} = 0.3$ – which is likely linked to the large fraction of low energetic film forming ions bombarding the growing coating surface, whilst the overall contribution from energetic Ti^{2+}-ions remains low (see Fig. 2). Consequently, this avoids the trapping of excess Ar interstitial atoms and reduces the point defect density [68]. In general, the presented evolution of the mechanical properties follows all previous interpretations on these coatings, yet again highlighting the excellent potential of R-HiPIMS deposited $Ti_{1-x}Al_xN$ thin films synthesised from composite targets.

4. Conclusion

In this work, the correlation between time-averaged and time-resolved ion fluxes to the N_2/Ar-flow-rate ratio utilised during reactive HiPIMS deposition of $Ti_{1-x}Al_xN$ thin films from $Ti_{0.4}Al_{0.6}$ or $Ti_{0.6}Al_{0.4}$ composite targets is studied. Detailed ion mass spectroscopy in the time- and energy-domain shows that for given discharge conditions the fraction of Al^+-ions is significantly affected by the Al/(Ti + Al)-ratio of the target material, whereas the amount of Ti^{n+}-ions ($n = 1, 2$) only shows a minor correlation to the target composition – despite the similar primary ionisation energies for Ti and Al. Moreover, resulting from progressing nitride formation, the data show a concomitant linear decrease for the total metal-to-gas-ion flux ratio J_{Me^+}/J_{g^+} with increasing N_2/Ar-flow-rate ratio, reducing J_{Me^+} from 36.3 and 29.6 % ($f_{[N2]}^{norm} = 0$) down to 15.4 and 15.6 % ($f_{[N2]}^{norm} = 1$) for the $Ti_{0.4}Al_{0.6}$ and $Ti_{0.6}Al_{0.4}$ target, respectively. Interestingly, Ti^{n+}-ion fractions remain almost unaffected by the applied N_2-flow-rate ratio, with the flux fractions of Ti^+- and Ti^{2+}-ions corresponding to less than 14 and 3 % of the total ionic flux from both targets,

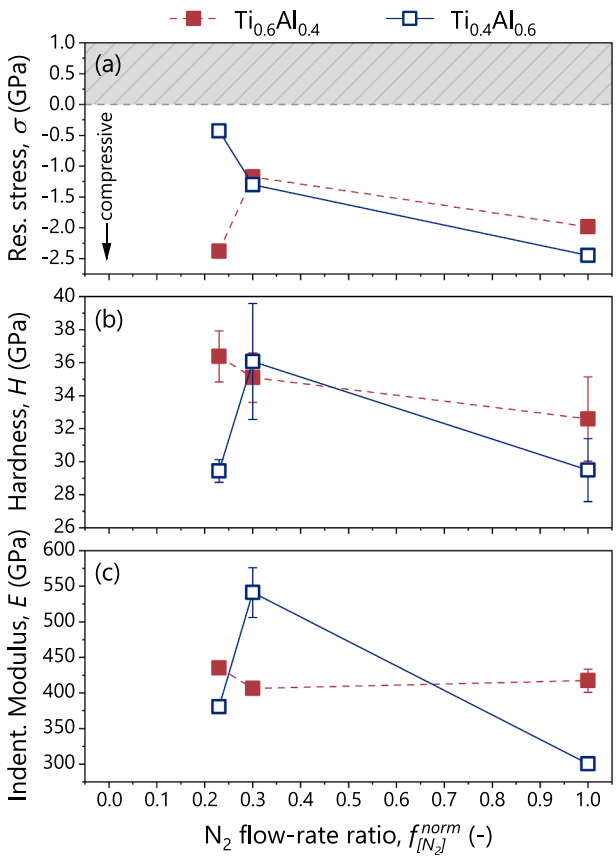

Fig. 7. (a) Biaxial residual stress, (b) nanoindentation hardness, as well as (c) nanoindentation modulus of all $Ti_{1-x}Al_xN$ thin films deposited onto (100)-oriented silicon substrates presented as function of $f^{norm}_{[N2]}$. Coatings deposited from $Ti_{0.6}Al_{0.4}$ cathodes are denoted by red, filled squares, whereas those from $Ti_{0.4}Al_{0.6}$ targets are indicated by blue, open squares.

respectively. Additional time-resolved ion distributions recorded for specific discharge conditions on the $Ti_{0.4}Al_{0.6}$ target confirm the fairly continuous arrival of both metal- and process-gas-ions throughout the entire HiPIMS pulse cycle, thus hinting at the reduced effectiveness of using synchronised bias potentials in tuning the film growth kinetics. Based on the recorded ion fluxes, predominantly cubic-structured $Ti_{1-x}Al_xN$ thin films with x_{max} as high as 0.63 could be synthesised – thoroughly proven by detailed structural analysis using XRD and TEM – exhibiting excellent mechanical properties (H up to ~36 GPa) at moderate stress states. This is realised by an increasing fraction of low-energy film forming ions present in the sputterred flux, while the fraction of energetic Ti^{2+} ions remains low. Thereby, the probability for trapped Ar interstitials and density of structural defects can be kept low.

Overall, the presented results show a clear pathway of controlling the ion flux composition and thin film structure during reactive HiPIMS deposition of $Ti_{1-x}Al_xN$ thin films from composite targets through the use of target-driven ion mass spectrosctopy.

CRediT authorship contribution statement

L. Zauner: Conceptualization, Investigation, Visualization, Writing – original draft. **A. Bahr:** Investigation, Writing – review & editing. **T. Kozák:** Investigation, Writing – review & editing. **J. Čapek:** Investigation, Writing – review & editing. **T. Wojcik:** Investigation, Writing – review & editing. **O. Hunold:** Writing – review & editing. **S. Kolozsvári:** Writing – review & editing. **P. Zeman:** Writing – review & editing. **P.H. Mayrhofer:** Writing – review & editing. **H. Riedl:** Supervision, Conceptualization, Writing – review & editing, Project administration.

Declaration of competing interest

The authors declare that they have no known competing financial interests or personal relationships that could have appeared to influence the work reported in this paper.

Acknowledgements

The financial support by the Austrian Federal Ministry for Digital and Economic Affairs, the National Foundation for Research, Technology and Development and the Christian Doppler Research Association is gratefully acknowledged (Christian Doppler Laboratory “Surface Engineering of high-performance Components”). The ion mass spectroscopy measurements done at University of West Bohemia were supported in part by the project LO 1506 of the Czech Ministry of Education, Youth and Sports under the program NPU I. We also thank for the financial support of Plansee SE, Plansee Composite Materials GmbH, and Oerlikon Balzers, Oerlikon Surface Solutions AG. In addition, we want to thank the X-ray center (XRC) of TU Wien for beam time as well as the electron microscopy center - USTEM TU Wien - for providing the SEM and TEM facilities. The authors acknowledge TU Wien Bibliothek for financial support through its Open Access Funding Programme.

Appendix A

Table A1
Detailed overview of the deposition parameters, chemical composition and mechanical properties of the synthesised coatings.

Coating	Target	$f^{norm}_{[N2]}$	p_{dep}	T_S	f	t_{on}	U_S	Al/Me	N	H	E	σ	dep. Rate
		[−]	[Pa]	[°C]	[Hz]	[μs]	[V]	[−]	[at.%]	[GPa]	[GPa]	[GPa]	[nm/min]
$Ti_{0.54}Al_{0.46}N$	$Ti_{0.6}Al_{0.4}$	0.23	0.4	300	500	75	−50	0.46	52.5	36.4 ± 1.6	435 ± 10	−2.4 ± 0.019	22.1
$Ti_{0.54}Al_{0.46}N$		0.3						0.46	53	35.1 ± 1.5	406 ± 10	−1.2 ± 0.004	17.4
$Ti_{0.58}Al_{0.42}N$		1						0.42	55	32.6 ± 2.6	417 ± 16	−2.0 ± 0.001	10.8
$Ti_{0.41}Al_{0.59}N$	$Ti_{0.4}Al_{0.6}$	0.23						0.59	38.5	29.4 ± 0.7	380 ± 10	−0.4 ± 0.003	66.2
$Ti_{0.37}Al_{0.63}N$		0.3						0.63	51	36.1 ± 3.5	541 ± 35	−1.3 ± 0.011	50.6
$Ti_{0.41}Al_{0.59}N$		1						0.59	53	29.5 ± 1.9	300 ± 9	−2.5 ± 0.012	10.9

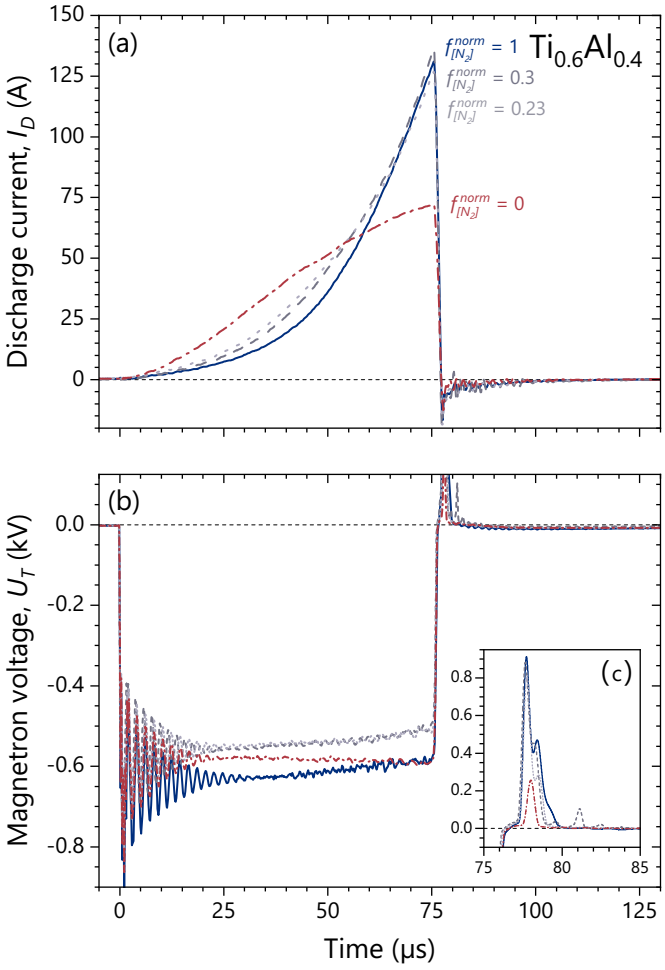

Fig. A1. Time-evolution of (a) the discharge current $I_D(t)$ and (b) the magnetron voltage on a $Ti_{0.6}Al_{0.4}$ target as functions of the applied nitrogen flow rate ratio $f^{norm}_{[N2]}$ for a pre-set pulse duration of 75 μs. Insert (c) shows details of the corresponding positive voltage overshoot recorded at the end of each pulse.

References

[1] D. Gall, C.S. Shin, T. Spila, M. Odén, M.J.H. Senna, J.E. Greene, I. Petrov, Growth of single-crystal CrN on MgO(001): effects of low-energy ion-irradiation on surface morphological evolution and physical properties, J. Appl. Phys. 91 (2002) 3589–3597, https://doi.org/10.1063/1.1446239.

[2] M. Lattemann, U. Helmersson, J.E. Greene, Fully dense, non-faceted 111-textured high power impulse magnetron sputtering TiN films grown in the absence of substrate heating and bias, Thin Solid Films 518 (2010) 5978–5980, https://doi.org/10.1016/j.tsf.2010.05.064.

[3] J.E. Greene, J.-E. Sundgren, L. Hultman, I. Petrov, D.B. Bergstrom, Development of preferred orientation in polycrystalline TiN layers grown by ultrahigh vacuum reactive magnetron sputtering ARTICLES YOU MAY BE INTERESTED IN, Appl. Phys. Lett. 67 (1995) 2928, https://doi.org/10.1063/1.114845.

[4] I. Petrov, P.B. Barna, L. Hultman, J.E. Greene, Microstructural evolution during film growth, J. Vac. Sci. Technol. A Vacuum, Surfaces, Film. 21 (2003) S117–S128, https://doi.org/10.1116/1.1601610.

[5] V. Kouznetsov, K. Macák, J.M. Schneider, U. Helmersson, I. Petrov, A novel pulsed magnetron sputter technique utilizing very high target power densities, Surf. Coat. Technol. 122 (1999) 290–293, https://doi.org/10.1016/S0257-8972(99)00292-3.

[6] J.T. Gudmundsson, N. Brenning, D. Lundin, U. Helmersson, High power impulse magnetron sputtering discharge, J. Vac. Sci. Technol. A 30 (2012), https://doi.org/10.1116/1.3691832, 030801.

[7] D. Lundin, J.T. Gudmundsson, T. Minea, High Power Impulse Magnetron Sputtering, Elsevier, 2020, https://doi.org/10.1016/C2016-0-02463-4.

[8] A.P. Ehiasarian, High-power impulse magnetron sputtering and its applications, Pure Appl. Chem. 82 (2010) 1247–1258, https://doi.org/10.1351/PAC-CON-09-10-43.

[9] K. Sarakinos, J. Alami, S. Konstantinidis, High power pulsed magnetron sputtering: a review on scientific and engineering state of the art, Surf. Coat. Technol. 204 (2010) 1661–1684, https://doi.org/10.1016/j.surfcoat.2009.11.013.

[10] A.P. Ehiasarian, A. Vetushka, Y.A. Gonzalvo, G. Sáfrán, L. Székely, P.B. Barna, Influence of high power impulse magnetron sputtering plasma ionization on the microstructure of TiN thin films, J. Appl. Phys. 109 (2011), 104314, https://doi.org/10.1063/1.3579443.
[11] T. Kozák, A.D. Pajdarová, M. Čada, Z. Hubička, P. Mareš, J. Čapek, Ion energy distributions at substrate in bipolar HiPIMS: effect of positive pulse delay, length and amplitude, Plasma Sources Sci. Technol. 29 (2020), 065003, https://doi.org/10.1088/1361-6595/ab8fbb.
[12] J.A. Santiago, I. Fernández-Martínez, T. Kozák, J. Capek, A. Wennberg, J. M. Molina-Aldareguia, V. Bellido-González, R. González-Arrabal, M.A. Monclús, The influence of positive pulses on HiPIMS deposition of hard DLC coatings, Surf. Coat. Technol. 358 (2019) 43–49, https://doi.org/10.1016/j.surfcoat.2018.11.001.
[13] Batková, J. Čapek, J. Rezek, R. Čerstvý, P. Zeman, Effect of positive pulse voltage in bipolar reactive HiPIMS on crystal structure, microstructure and mechanical properties of CrN films Surf. Coat. Technol. 393 (2020) 125773. doi:https://doi.org/10.1016/j.surfcoat.2020.125773.
[14] G. Greczynski, J. Jensen, J. Böhlmark, L. Hultman, Microstructure control of CrNx films during high power impulse magnetron sputtering, Surf. Coat. Technol. 205 (2010) 118–130, https://doi.org/10.1016/j.surfcoat.2010.06.016.
[15] A. Anders, Tutorial: reactive high power impulse magnetron sputtering (R-HiPIMS), J. Appl. Phys. 121 (2017), 171101, https://doi.org/10.1063/1.4978350.
[16] S.M. Rossnagel, Gas density reduction effects in magnetrons, J. Vac. Sci. Technol. A Vacuum, Surfaces, Film. 6 (1988) 19–24, https://doi.org/10.1116/1.574988.
[17] A. Anders, J. Čapek, M. Hála, L. Martinu, The 'recycling trap': a generalized explanation of discharge runaway in high-power impulse magnetron sputtering, J. Phys. D. Appl. Phys. 45 (2012), 012003, https://doi.org/10.1088/0022-3727/45/1/012003.
[18] J. Čapek, S. Kadlec, Return of target material ions leads to a reduced hysteresis in reactive high power impulse magnetron sputtering: experiment, J. Appl. Phys. 121 (2017), 171911, https://doi.org/10.1063/1.4977816.
[19] A. Anders, Discharge physics of high power impulse magnetron sputtering, Surf. Coat. Technol. 205 (2011) S1–S9, https://doi.org/10.1016/J.SURFCOAT.2011.03.081.
[20] L. Zauner, P. Ertelthaler, T. Wojcik, H. Bolvardi, S. Kolozsvári, P.H. Mayrhofer, H. Riedl, Reactive HiPIMS deposition of Ti-Al-N: influence of the deposition parameters on the cubic to hexagonal phase transition, Surf. Coat. Technol. 382 (2020), 125007, https://doi.org/10.1016/j.surfcoat.2019.125007.
[21] J. Paulitsch, P.H. Mayrhofer, W.D. Münz, M. Schenkel, Structure and mechanical properties of CrN/TiN multilayer coatings prepared by a combined HIPIMS/UBMS deposition technique, Thin Solid Films 517 (2008) 1239–1244, https://doi.org/10.1016/j.tsf.2008.06.080.
[22] M. Samuelsson, D. Lundin, J. Jensen, M.A. Raadu, J.T. Gudmundsson, U. Helmersson, On the film density using high power impulse magnetron sputtering, Surf. Coat. Technol. 205 (2010) 591–596, https://doi.org/10.1016/j.surfcoat.2010.07.041.
[23] T. Shimizu, H. Komiya, Y. Teranishi, K. Morikawa, H. Nagasaka, M. Yang, Pressure dependence of (Ti, Al)N film growth on inner walls of small holes in high-power impulse magnetron sputtering, Thin Solid Films 624 (2017) 189–196, https://doi.org/10.1016/j.tsf.2016.09.041.
[24] M. Balzer, M. Fenker, Three-dimensional thickness and property distribution of TiC films deposited by DC magnetron sputtering and HIPIMS, Surf. Coat. Technol. 250 (2014) 37–43, https://doi.org/10.1016/j.surfcoat.2014.02.011.
[25] G. Greczynski, I. Zhirkov, I. Petrov, J.E. Greene, J. Rosen, Control of the metal/gas ion ratio incident at the substrate plane during high-power impulse magnetron sputtering of transition metals in Ar, Thin Solid Films 642 (2017) 36–40, https://doi.org/10.1016/j.tsf.2017.09.027.
[26] G. Greczynski, I. Petrov, J.E. Greene, L. Hultman, Strategy for tuning the average charge state of metal ions incident at the growing film during HIPIMS deposition, Vacuum. 116 (2015) 36–41, https://doi.org/10.1016/j.vacuum.2015.02.027.
[27] D. Lundin, M. Čada, Z. Hubička, Ionization of sputtered Ti, Al, and C coupled with plasma characterization in HiPIMS, Plasma Sources Sci. Technol. 24 (2015), 035018, https://doi.org/10.1088/0963-0252/24/3/035018.
[28] N. Britun, S. Konstantinidis, R. Snyders, An overview on time-resolved optical analysis of HiPIMS discharge, Plasma Process. Polym. 12 (2015) 1010–1027, https://doi.org/10.1002/ppap.201500051.
[29] G. Greczynski, L. Hultman, Time and energy resolved ion mass spectroscopy studies of the ion flux during high power pulsed magnetron sputtering of Cr in Ar and Ar/N2 atmospheres, Vacuum. 84 (2010) 1159–1170, https://doi.org/10.1016/j.vacuum.2010.01.055.
[30] M. Palmucci, N. Britun, T. Silva, R. Snyders, S. Konstantinidis, Mass spectrometry diagnostics of short-pulsed HiPIMS discharges, J. Phys. D. Appl. Phys. 46 (2013), 215201, https://doi.org/10.1088/0022-3727/46/21/215201.
[31] A. Ferrec, J. Keraudy, S. Jacq, F. Schuster, P.Y. Jouan, M.A. Djouadi, Correlation between mass-spectrometer measurements and thin film characteristics using dcMS and HiPIMS discharges, Surf. Coat. Technol. 250 (2014) 52–56, https://doi.org/10.1016/j.surfcoat.2014.02.030.
[32] J. Bohlmark, M. Lattemann, J.T. Gudmundsson, A.P. Ehiasarian, Y. Aranda Gonzalvo, N. Brenning, U. Helmersson, The ion energy distributions and ion flux composition from a high power impulse magnetron sputtering discharge, Thin Solid Films 515 (2006) 1522–1526, https://doi.org/10.1016/j.tsf.2006.04.051.
[33] G. Greczynski, I. Zhirkov, I. Petrov, J.E. Greene, J. Rosen, Time evolution of ion fluxes incident at the substrate plane during reactive high-power impulse magnetron sputtering of groups IVb and VIb transition metals in Ar/N 2, J. Vac. Sci. Technol. A 36 (2018), 020602, https://doi.org/10.1116/1.5016241.
[34] G. Greczynski, J. Lu, M.P. Johansson, J. Jensen, I. Petrov, J.E. Greene, L. Hultman, Role of tin+ and Aln+ ion irradiation (n=1, 2) during Ti1-xAlxN alloy film growth in a hybrid HIPIMS/magnetron mode, Surf. Coat. Technol. 206 (2012) 4202–4211, https://doi.org/10.1016/j.surfcoat.2012.04.024.
[35] G. Greczynski, I. Petrov, J.E. Greene, L. Hultman, Paradigm shift in thin-film growth by magnetron sputtering: from gas-ion to metal-ion irradiation of the growing film, J. Vac. Sci. Technol. A 37 (2019), 060801, https://doi.org/10.1116/1.5121226.
[36] G. Greczynski, S. Mráz, M. Hans, J. Lu, L. Hultman, J. Schneider, Control over the phase formation in metastable transition metal nitride thin films by tuning the Al+ subplantation depth, Coatings. 9 (2018) 17, https://doi.org/10.3390/coatings9010017.
[37] M. Lattemann, A.P. Ehiasarian, J. Bohlmark, P.Å.O. Persson, U. Helmersson, Investigation of high power impulse magnetron sputtering pretreated interfaces for adhesion enhancement of hard coatings on steel, Surf. Coat. Technol. 200 (2006) 6495–6499, https://doi.org/10.1016/j.surfcoat.2005.11.082.
[38] A.P. Ehiasarian, J.G. Wen, I. Petrov, Interface microstructure engineering by high power impulse magnetron sputtering for the enhancement of adhesion, J. Appl. Phys. 101 (2007), https://doi.org/10.1063/1.2697052.
[39] G. Greczynski, J. Lu, J. Jensen, I. Petrov, J.E. Greene, S. Bolz, W. Kölker, C. Schiffers, O. Lemmer, L. Hultman, Metal versus rare-gas ion irradiation during Ti1-xAlxN film growth by hybrid high power pulsed magnetron/dc magnetron co-sputtering using synchronized pulsed substrate bias, J. Vac. Sci. Technol. A 30 (2012), 061504, https://doi.org/10.1116/1.4750485.
[40] N. Nedfors, O. Vozniy, J. Rosen, Effect of synchronized bias in the deposition of TiB 2 thin films using high power impulse magnetron sputtering, J. Vac. Sci. Technol. A Vacuum, Surfaces, Film. 36 (2018), 031510, https://doi.org/10.1116/1.5003194.
[41] B. Bakhit, I. Petrov, J.E. Greene, L. Hultman, J. Rosén, G. Greczynski, Controlling the B/Ti ratio of TiB x thin films grown by high-power impulse magnetron sputtering, J. Vac. Sci. Technol. A Vacuum, Surfaces, Film. 36 (2018), 030604, https://doi.org/10.1116/1.5026445.
[42] W. Münz, Titanium aluminum nitride films: a new alternative to TiN coatings, J. Vac. Sci. Technol. A 4 (1986) 2717–2725, https://doi.org/10.1116/1.573713.
[43] O. Knotek, T. Leyendecker, On the structure of (Ti, Al)N-PVD coatings, J. Solid State Chem. 70 (1987) 318–322, https://doi.org/10.1016/0022-4596(87)90071-5.
[44] P.H. Mayrhofer, D. Music, J.M. Schneider, Influence of the Al distribution on the structure, elastic properties, and phase stability of supersaturated Ti1−xAlxN, J. Appl. Phys. 100 (2006), 094906, https://doi.org/10.1063/1.2360778.
[45] L. Chen, Y. Du, P.H. Mayrhofer, S.Q. Wang, J. Li, The influence of age-hardening on turning and milling performance of Ti-Al-N coated inserts, Surf. Coat. Technol. 202 (2008) 5158–5161, https://doi.org/10.1016/j.surfcoat.2008.05.036.
[46] L. Chen, M. Moser, Y. Du, P.H. Mayrhofer, Compositional and structural evolution of sputtered Ti-Al-N, Thin Solid Films 517 (2009) 6635–6641, https://doi.org/10.1016/j.tsf.2009.04.056.
[47] K. Kutschej, P.H. Mayrhofer, M. Kathrein, P. Polcik, R. Tessadri, C. Mitterer, Structure, mechanical and tribological properties of sputtered Ti1-xAlxN coatings with $0.5 \leq x \leq 0.75$, Surf. Coat. Technol. 200 (2005) 2358–2365, https://doi.org/10.1016/j.surfcoat.2004.12.008.
[48] L. Chen, J. Paulitsch, Y. Du, P.H. Mayrhofer, Thermal stability and oxidation resistance of Ti–Al–N coatings, Surf. Coat. Technol. 206 (2012) 2954–2960, https://doi.org/10.1016/j.surfcoat.2011.12.028.
[49] G. Greczynski, J. Lu, J. Jensen, S. Bolz, W. Kölker, C. Schiffers, O. Lemmer, J. E. Greene, L. Hultman, A review of metal-ion-flux-controlled growth of metastable TiAlN by HIPIMS/DCMS co-sputtering, Surf. Coat. Technol. 257 (2014) 15–25, https://doi.org/10.1016/j.surfcoat.2014.01.055.
[50] C.L. Chang, F.C. Yang, Effect of target composition on the microstructural, mechanical, and corrosion properties of TiAlN thin films deposited by high-power impulse magnetron sputtering, Surf. Coat. Technol. 352 (2018) 330–337, https://doi.org/10.1016/j.surfcoat.2018.08.023.
[51] S. Severin, M. Naveed, S. Weiß, Effect of HPPMS pulse-frequency on plasma discharge and deposited AlTiN coating properties, Adv. Mater. Sci. Eng. (2017) 18, https://doi.org/10.1155/2017/4850908.
[52] G. Greczynski, S. Mráz, M. Hans, D. Primetzhofer, J. Lu, L. Hultman, J. M. Schneider, Unprecedented Al supersaturation in single-phase rock salt structure VAlN films by Al+subplantation, J. Appl. Phys. 121 (2017), 171907, https://doi.org/10.1063/1.4977813.
[53] G. Greczynski, S. Mráz, L. Hultman, J.M. Schneider, Selectable phase formation in VAlN thin films by controlling Al+ subplantation depth, Sci. Rep. 7 (2017) 17544, https://doi.org/10.1038/s41598-017-17846-5.
[54] D.R. Lide, CRC Handbook of Chemistry and Physics, 84th ed., CRC Press, 2003.
[55] Hiden Analytical Ltd. EQP and EQS Analysers, (n.d.). https://www.hiden.de/wp-content/uploads/pdf/EQP_and_EQS_-_Hiden_Analytical_Techinical_Inofrmation.pdf (accessed November 26, 2020).
[56] Private communications between Hiden Analytical Ltd. and T. Kozák, (2019).
[57] M. Klinger, A. Jäger, Crystallographic tool box (CrysTBox): automated tools for transmission electron microscopists and crystallographers, J. Appl. Crystallogr. 48 (2015) 2012–2018, https://doi.org/10.1107/S1600576715017252.
[58] G.M. Pharr, An improved technique for determining hardness and elastic modulus using load and displacement sensing indentation experiments, J. Mater. Res. 7 (1992) 1564–1583, https://doi.org/10.1557/JMR.1992.1564.
[59] G.C.A.M. Janssen, M.M. Abdalla, F. van Keulen, B.R. Pujada, B. van Venrooy, Celebrating the 100th anniversary of the Stoney equation for film stress: developments from polycrystalline steel strips to single crystal silicon wafers, Thin Solid Films 517 (2009) 1858–1867, https://doi.org/10.1016/j.tsf.2008.07.014.

[60] D. Depla, X.Y. Li, S. Mahieu, R. De Gryse, Determination of the effective electron emission yields of compound materials, J. Phys. D. Appl. Phys. 41 (2008), https://doi.org/10.1088/0022-3727/41/20/202003.
[61] F. Magnus, O.B. Sveinsson, S. Olafsson, J.T. Gudmundsson, Current-voltage-time characteristics of the reactive Ar/N 2 high power impulse magnetron sputtering discharge, J. Appl. Phys. 110 (2011), 083306, https://doi.org/10.1063/1.3653233.
[62] J.Y. Rauch, C. Rousselot, N. Martin, Structure and composition of TixAll-xN thin films sputter deposited using a composite metallic target, Surf. Coat. Technol. 157 (2002) 138–143, https://doi.org/10.1016/S0257-8972(02)00146-9.
[63] S. Inoue, H. Uchida, A. Hioki, K. Koterazawa, R.P. Howson, Structure and composition of (Ti, Al)N films prepared by r.f. planar magnetron sputtering using a composite target, Thin Solid Films 271 (1995) 15–18, https://doi.org/10.1016/0040-6090(95)06817-1.
[64] A.D. Pajdarová, J. Vlček, P. Kudláček, J. Lukáš, Electron energy distributions and plasma parameters in high-power pulsed magnetron sputtering discharges, Plasma Sources Sci. Technol. 18 (2009), https://doi.org/10.1088/0963-0252/18/2/025008, 025008.
[65] ICDD, Powder Diffraction File - wurtzite AlN - 04-016-3965, (2013).
[66] D. Gall, S. Kodambaka, M.A. Wall, I. Petrov, J.E. Greene, Pathways of atomistic processes on TiN(001) and (111) surfaces during film growth: an ab initio study, J. Appl. Phys. 93 (2003) 9086–9094, https://doi.org/10.1063/1.1567797.
[67] L. Hultman, J.E. Sundgren, J.E. Greene, Formation of polyhedral N 2 bubbles during reactive sputter deposition of epitaxial TiN(100) films, J. Appl. Phys. 66 (1989) 536–544, https://doi.org/10.1063/1.343570.
[68] G. Greczynski, J. Lu, J. Jensen, I. Petrov, J.E. Greene, S. Bolz, W. Kölker, C. Schiffers, O. Lemmer, L. Hultman, Strain-free, single-phase metastable Ti0.38Al0.62N alloys with high hardness: metal-ion energy vs. momentum effects during film growth by hybrid high-power pulsed/dc magnetron cosputtering, Thin Solid Films 556 (2014) 87–98, https://doi.org/10.1016/j.tsf.2014.01.017.
[69] ICDD, Powder diffraction file - cubic TiN - 00-038-1420, (1970).
[70] ICDD, Powder diffraction file - cubic AlN - 00-025-1495, (1970).
[71] ICDD, Powder diffraction file - cubic Si - 00-027-1402, (2017) 7–8.